Figure 7

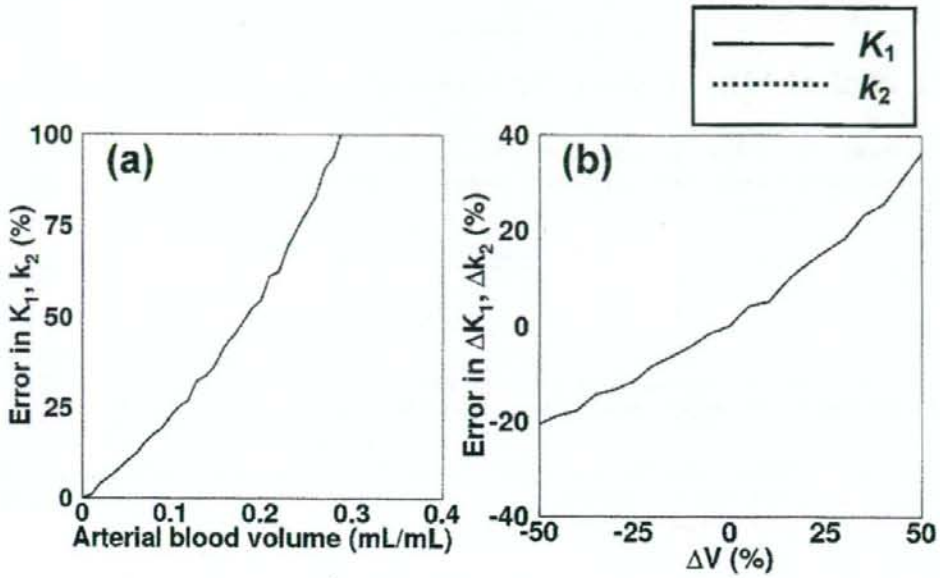
K_1
k_2
(a)
(b)
Error in K_1, k_2 (%)
Arterial blood volume (mL/mL)
Error in ΔK_1, Δk_2 (%)
ΔV (%)
100
75
50
25
0
0
0.1
0.2
0.3
0.4
40
20
0
-20
-40
-50
-25
0
25
50

Radiol Phys Technol
DOI 10.1007/s12194-008-0038-x

Use of a clinical MRI scanner for preclinical research on rats

Akihide Yamamoto · Hiroshi Sato · Jun-ichiro Enmi · Kenji Ishida · Takayuki Ose · Atsuomi Kimura · Hideaki Fujiwara · Hiroshi Watabe · Takuya Hayashi · Hidehiro Iida

Received: 27 May 2008 / Revised: 22 August 2008 / Accepted: 27 August 2008

Abstract This study evaluated the feasibility of imaging rat brains using a human whole-body 3-T magnetic resonance imaging (MRI) scanner with specially developed transmit-and-receive radiofrequency coils. The T_1- and T_2-weighted images obtained showed reasonable contrast. Acquired contrast-free time-of-flight magnetic resonance angiography images clearly showed the cortical middle cerebral artery (MCA) branches, and interhemispheric differences could be observed. Dynamic susceptibility contrast MRI at 1.17 mm^3 voxel resolution, performed three times following administration of gadolinium diethylenetriamine pentaacetic acid (Gd-DTPA, 0.1 mmol/kg), demonstrated that the arterial input function (AIF) can be obtained from the MCA region, yielding cerebral blood flow (CBF), cerebral blood volume, and mean transit time (MTT) maps. The hypothalamus (HT) to parietal cortex (Pt) CBF ratio was 45.11 ± 2.85%, and the MTT was 1.29 ± 0.40 s in the Pt region and 2.32 ± 0.17 s in the HT region. A single dose of Gd-DTPA enabled the assessment of AIF within MCA territory and of quantitative CBF in rats.

Keywords Quantitative mapping · Human whole-body 3-T MRI scanner · Single dose of Gd-DTPA · Dynamic susceptibility contrast (DSC) · Preclinical research · Rat brain

A. Yamamoto · J. Enmi · K. Ishida · T. Ose · H. Watabe · T. Hayashi · H. Iida (✉)
Department of Investigative Radiology,
Advanced Medical Engineering Center,
National Cardiovascular Center Research Institute,
5-7-1, Fujishiro-dai, Suita, Osaka 565-8565, Japan
e-mail: iida@ri.ncvc.go.jp

A. Yamamoto · A. Kimura · H. Fujiwara · H. Watabe · T. Hayashi · H. Iida
Department of Medical Physics and Engineering,
Division of Health Sciences, Graduate School of Medicine,
Osaka University, 1-7, Yamada-oka, Suita,
Osaka 565-0871, Japan

H. Sato
Laboratory for Diagnostic Solution,
Advanced Medical Engineering Center,
National Cardiovascular Center Research Institute,
5-7-1, Fujishiro-dai, Suita, Osaka 565-8565, Japan

1 Introduction

Magnetic resonance imaging (MRI) has been widely used in preclinical research on experimental small animals. Studies have typically been aimed at understanding the pathophysiologic status and evaluating the efficacy/side effects of newly developed treatments, such as pharmaceutical and regenerative medicine. Recently, a different idea has surfaced: the use of a human whole-body MRI scanner for small-animal imaging [1]. Although small-animal-dedicated scanners are superior to clinical scanners in terms of providing a better signal-to-noise ratio, the available pulse sequences are different from those in clinical scanners, and the magnetic field strength is often much higher. Small-animal imaging with clinical scanners is important for directly addressing clinical questions and/or identifying the origins of signal changes, including various disease conditions in a clinical setting.

Smith et al. [2] demonstrated that anatomic brain T_1- weighted (T_1W) images and T_2-weighted (T_2W) images can be obtained for healthy rats by using a 1-T clinical MRI scanner with a specially designed radiofrequency (RF) coil, given a reasonable spatial resolution (0.1953 × 0.1953 × 2.5 mm, 24 min of T_1W and 48 min of T_2W). The image contrast was sufficiently high to

distinguish the cortical gray matter from the white matter [corpus callosum (CC)], as well as the lateral ventricle (LV) and interpeduncular cistern (IPC) from the thalamus (Thal). Guzman et al. [3] employed a clinical 1.5-T MRI scanner with a commercially available RF coil and demonstrated that both T_1W and T_2W images can be obtained with good contrast, a reasonable spatial resolution of $0.3125 \times 0.3125 \times 1.5$ mm, and an acquisition time of 19 min 51 s, as well as $0.35156 \times 0.375 \times 1.5$ mm at 8 min 34 s, corresponding to T_1W and T_2W images, respectively. Other investigators [4] applied a clinical 1.5-T MRI scanner with a 3-in.-diameter circular receive-only surface coil to assess anatomic images. Their images can be used to evaluate the pathophysiologic status of stroke [4] and cancer [5, 6], as well as the effects of neural excitotoxicity [3]. There were also several studies that used a clinical 3-T MRI scanner fitted with commercial and/or hand-made RF coils to investigate the pathophysiology of stroke [7, 8] and brain tumors in rats [6, 9, 10]. Generally speaking, anatomic images with better contrast can be obtained in a stronger magnetic field, although there are additional factors that may influence the signal-to-noise ratio (SNR) or spatial resolution of anatomic images. Contrast-free time-of-flight magnetic-resonance angiography (TOF-MRA) can also be performed on rats; a reasonable spatial resolution was obtained by using a clinical 3-T MRI scanner with a single-turn solenoid coil [11].

Dynamic susceptibility contrast MRI (DSC-MRI) [12] has been widely used in clinical diagnosis, particularly in patients with stroke [13–19] and tumors [20]. The application of clinical MRI scanners has been extended to DSC-MRI studies of small animals with stroke [21, 22] and tumors [23] using a 1.5-T MRI scanner. Up to now, small-animal studies have been performed on 1.5-T MRI scanners only, and 3-T scanners have not been employed so far. This is largely attributed to the fact that the susceptibility-induced inhomogeneous magnetic field can cause more serious distortion of the images at a higher static magnetic field. In DSC-MRI studies, the echo planar imaging (EPI) technique is mainly used because fast acquisition is required for accurate tracking of the bolus passage of MR contrast agents. The EPI technique, however, is very sensitive to magnetic field inhomogeneity, and thus the EPI images of small-animal brains may be severely distorted. The gradient slew rate (SR) is not high enough to support a sufficiently short echo spacing period when clinical scanners are used for high spatial resolution imaging of small objects. Moreover, injected materials may cause further distortion [24]. The degree of distortion of dynamic EPI images of small-animal brains produced by a 3-T clinical scanner is currently unknown. The arterial input function (AIF) is also questionable. To the best of our knowledge, no DSC-MRI studies of small-animal brains on 3-T clinical scanners have been reported.

This study attempted to evaluate the feasibility of developing a human whole-body 3-T MRI system for small animals, particularly DSC-MRI with a single dose of gadolinium-diethylenetriamine pentaacetic acid (Gd-DTPA). The quality of various images—including the anatomic T_1W images, T_2W images, time-of-flight magnetic resonance angiography (TOF-MRA) images and DSC images—was tested, and the availability of the AIF obtained from rat brain was evaluated.

2 Materials and methods

2.1 Subjects

The subjects were three healthy adult rats supplied by Japan SLC, Inc. (Shizuoka, Japan). All three rats were males, and they ranged in age from 20 to 24 weeks. Their weight range was between 400 and 600 g. Anesthesia was administered with an intramuscular injection of ketamine (33 mg/kg; Daiichi-Sankyo Co., Ltd., Tokyo, Japan) and xylazine (6.6 mg/kg; Bayer Yakuhin, Ltd., Osaka, Japan). The first rat (Sprague Dawley, SD) was used for T_1-W and T_2W imaging of the whole brain. The second rat, also a SD, was used for contrast-free TOF-MRA imaging. The third was a Wistar rat, which was used for a Gd-DTPA (0.1 mmol/kg; Bayer Yakuhin, Ltd., Osaka, Japan)-enhanced DSC-MRI sequence. Experiments were carried out according to the protocol approved by the Local Committee for Laboratory Animal Welfare, National Cardiovascular Center, Osaka, Japan.

2.2 MRI acquisition

A human whole-body 3-T MRI scanner (Signa, GE Healthcare, Milwaukee, WI, USA) equipped with a 55-cm bore was employed in this study. The gradient coil system was capable of providing a maximum gradient amplitude of 40 mT/m and an SR of 150 T m^{-1} s^{-1}. All sequence programs employed in this study were designed for clinical studies.

Two solenoid coils designed for rats were specially developed to cover the whole brain, and were capable of both transmitting and receiving RF pulses. The three-turn solenoid coil, which had a diameter of 42 mm and a length along its cylindrical axis of 18 mm, was attached to an apparatus made from an acrylic mold, as shown in Fig. 1. All components of the stereotaxic apparatus consisted of nonmagnetic materials that fixed the head positions of the rats during data acquisition. The RF coil was designed to have an impedance of 50 Ω at a resonance frequency of

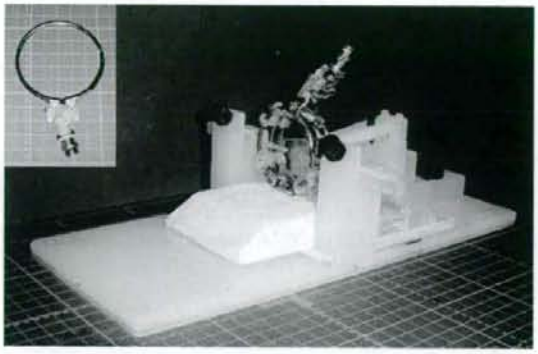

Fig. 1 The head fixation system for small animals, which was fitted with an MRI coil for RF transmission and reception. The coil is typically a three-turn solenoid; it can also be a single-turn coil, as shown on the *top left* of this figure

127.76 MHz. An additional single-turn surface coil of diameter 62 mm diameter was also developed for better homogeneity and was used for a single slice of DSC-MRI. The RF power in these coils had to be reduced to less than that used in the standard human head coil because of the diameter of the small coil. The transmission signal was therefore attenuated to 20 dB, which allowed the use of automated scanner software, including the calibration of the RF transmission power and receiver gains. All rats were fixed on the stereotaxic apparatus. They were placed at the center of the gantry and oriented with the craniocaudal axis perpendicular to the static magnetic field. Their heads were positioned inside the coil along the craniocaudal direction.

T_1W images were obtained with a conventional two-dimensional fast spin echo (2D-FSE) sequence. The repetition time (TR) was 1,500 ms [10]. The echo time (TE) was fixed at 14 ms. The echo train length (ETL) was 3. The field of view (FOV) was set at 40 × 30 mm^2, the slice thickness at 1.5 mm, the slice gap at 0.5 mm, the number of excitations (NEX) at 10, and the band width (BW) at 31.3 kHz. The acquired matrix (256 × 160) was interpolated, and null pixels were added in k-space to produce square matrices of 256 × 256. The acquisition time was 10 min 3 s.

T_2W images were obtained with a 2D-FSE and the following imaging parameters: TR, 4,100 ms; TE, 128 ms; ETL, 14; FOV, 40 × 30 mm; slice thickness, 1.5 mm; slice gap, 0.5 mm; NEX, 8; BW, 31.3 kHz; acquired matrix, 256 × 160, zero-filled to 256 × 256; phase direction, ventral-dorsal; acquisition time, 11 min 2 s.

Time-of-flight magnetic resonance angiography was performed using a three-dimensional flow-compensated spoiled gradient recalled (3D-SPGR) sequence prepared with magnetization transfer and with: TR, 53 ms; TE, 5.5 ms; flip angle (FA), 45°; BW, 16 kHz; FOV, 8 × 6 cm; slice thickness, 0.2 mm; one acquired slab of 512 × 512 × 64; voxel resolution, 0.156 × 0.156 × 0.2 mm^3; NEX, 1; acquisition time, 21 min 46 s.

Dynamic susceptibility contrast images were obtained following the intravenous administration of Gd-DTPA to the T_2*-weighted gradient echo dynamic images. A bolus of Gd-DTPA (0.1 mmol/kg) was injected manually into the tail vein with a 22-gauge catheter via 1 m of polyethylene tubing (PE50, internal diameter: 0.58 mm/outer diameter: 0.965 mm, Becton Dickinson and Company, Franklin Lakes, NJ, USA), and was followed by an additional administration of saline (1.0 ml). A multishot EPI (number of shots = 2) was employed to improve EPI distortion and temporal resolution. The imaging parameters were: TR, 142 ms; TE, 22.1 ms; FA, 20°; FOV, 40 × 40 mm; matrix size, 64 × 64, leading to a pixel size of 0.625 × 0.625 mm^2. The slice thickness was 3 mm in a single slice around the hypothalamus (HT). The temporal resolution was 0.284 s per image, and the acquisition time was 1 min 15 s. This assessment was repeated three times at intervals of 40 min and 10 min, corresponding to the first–second and second–third scans, respectively.

2.3 Data analysis

All MRI images were reconstructed on the same workstation provided for the GE Signa 3-T scanner used for the clinical programs. The images were then transferred to a Linux workstation. Lastly, data analysis was carried out using in-house and commercial software.

To evaluate the T_1W and T_2W image quality, we calculated the contrast-to-noise ratio (CNR) with an inter-tissue method [25–27] as follows: $CNR = (\pi/2)^{1/2} (SI_a - SI_b)/SI_{air}$, where SI_{air} represents the mean signal intensity of air, and SI_a and SI_b represent the signal intensities of tissue a and tissue b, respectively.

Angiograms were created by generating the partial maximum intensity projection (MIP) with commercial software [Virtual Place Liberty (VPL), AZE Co. Ltd., Tokyo, Japan]. Visible middle cerebral artery (MCA) branches and left-to-right differences in MCA were carefully investigated.

For the DSC images of slice sections containing the internal carotid artery (ICA) and/or MCA, a series of images were carefully observed. A region of interest (ROI) was carefully selected in the MCA region, from which the AIF was obtained, with the help of other anatomic information. To avoid susceptibility artifacts caused by air in the trachea, the area of the arterial circle of Willis was excluded from the definition of the AIF. The anterior cerebral artery was also excluded because of possible susceptibility effects attributed to venous blood. A Gaussian filter of full width at half maximum (FWHM) 1.1 mm

was applied to all dynamic images. The time versus signal intensity curves (TICs) were converted to the Gd-DTPA concentration according to Eq. 1 given in the "Appendix." Functional mapping images of the mean transit time (MTT), cerebral blood volume (CBV), and cerebral blood flow (CBF) were carried out with the deconvolution method [28]. The theory behind this is described in detail in the "Appendix." For ROI analysis, images of matrix size 64 × 64 were converted to 256 × 256 using a sinc interpolation function.

3 Results

T_1W and T_2W images reconstructed with a spatial resolution of 0.156 × 0.188 × 1.5 mm are shown in Fig. 2. White matter could be discriminated from cortical and deep gray matter regions. The locations of small anatomic features such as the caudate putamen (CPu), striatum, the CC, and the hippocampus (HC) could also be identified in both T_1W and T_2W anatomic images. The CNRs between the HC and CC were 15.6 and 9.8, respectively, for the T_1W and T_2W images shown in Fig. 2. The CNRs between the HC and IC were 23.2 and 13.6, respectively, although the CNR may be underestimated due to the contamination of signal from the globus pallidus.

Results for MIP images obtained with contrast-free TOF-MRA are shown in Fig. 3. Coronal MIP images around the HT of thickness 5 mm are shown in Fig. 3a. In this figure, the slice section contained ICAs and MCA. The MCA, the cortical branches in both the left and right hemispheres, can be identified. It is important to note that the anatomic structure of the cortical MCA arteries is different between the right and left hemispheres. The ROI for the AIF was selected in the MCA region and is shown by the arrows in Fig. 3a and b.

A typical example of a DSC-MRI image is shown in Fig. 4. Distortion of the DSC-MRI images is visible in Fig. 4A in the phase direction. A magnified area from dynamic images of the MCA region (shown as a rectangle in Fig. 4A) is displayed in Fig. 4B. Several pixels indicate temporal changes in pixel contrast as a function of time, and these are reflected by Gd-DTPA negative enhancement. The pixel signal intensity varied as shown in Fig. 4C, and the curve shown was employed to estimate the AIF. Figure 5 shows the TIC in this area together with the TIC for the whole brain region obtained from each of the three scans. The curves were visually reproducible in terms of the shapes, heights and widths of the curves around the peak, as well as the tail height at the end of the scan. It should also be noted that the baseline was consistent before each injection of Gd-DTPA, even though the second and

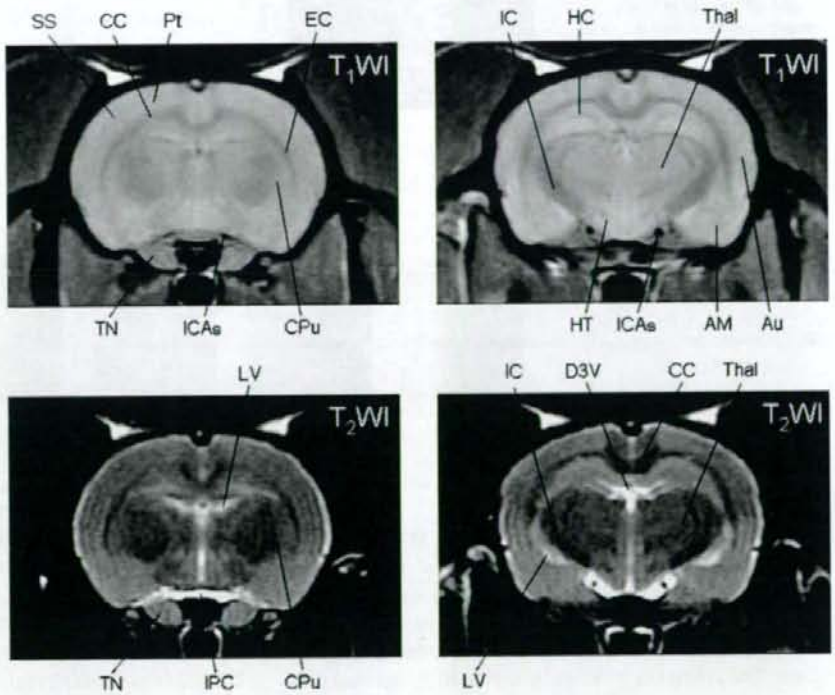

Fig. 2 T_1W images (*top*) and T_2W images (*bottom*) obtained from an SD rat, with the following anatomic locations as indicated: the somatosensory cortex (*SS*), corpus callosum (*CC*), parietal cortex (*Pt*), external capsule (*EC*), caudate putamen (*CPu*), internal capsule (*IC*), hippocampus (*HC*), thalamus (*Thal*), auditory cortex (*Au*), amygdala (*AM*), hypothalamus (*HT*), internal carotid arterial system (*ICAs*), trigeminal nerve (*TN*), interpeduncular cistern (*IPC*), dorsal third ventricle (*D3V*), and the lateral ventricle (*LV*). These slice sections were located −1.5 mm (*left*) and −3.5 mm (*right*), respectively, from the bregma

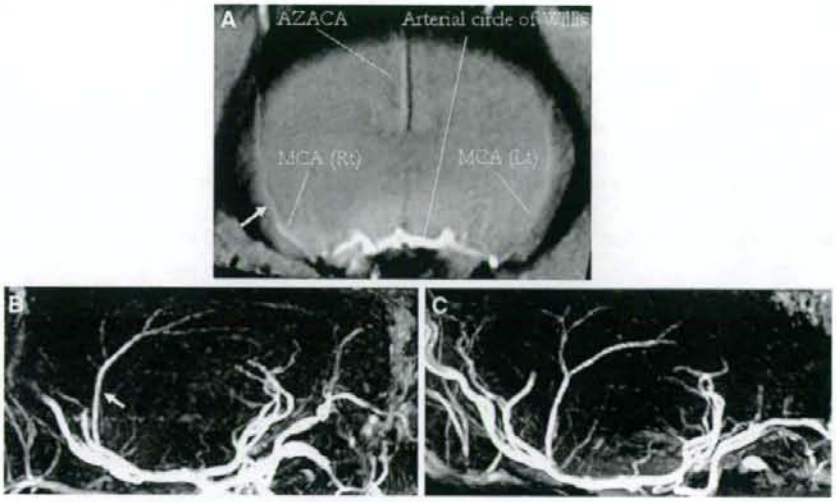

Fig. 3 Partial maximum intensity projection maps of contrast-free time-of-flight MRA obtained for a Sprague Dawley rat. Maps represent areas around the Thal (**a**), right hemisphere (**b**), and left hemisphere (**c**). The *white arrows* indicate the selected ROI level (as described in the "Discussion"). *AZACA*, azygos anterior cerebral artery

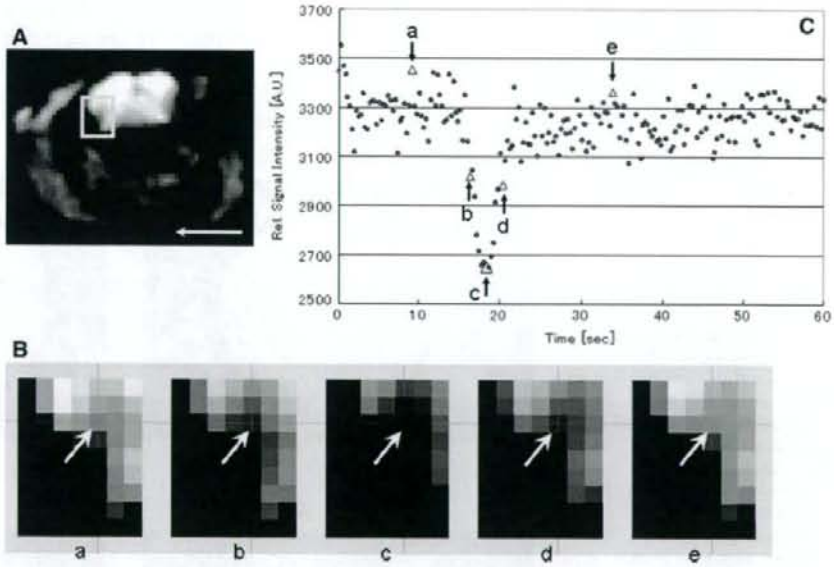

Fig. 4 Typical time-frame images obtained from Gd-bolus tracking T_2*-weighted dynamic images (after the first injection). A *white rectangle* was placed in the MCA area (**a**), and magnified images of this rectangle were visualized as *a*, *b*, *c*, *d*, and *e* in **b**. The TIC within the pixels is indicated by *white arrows* in **b**. The data were then plotted in a graph (**c**). Typical data points were extracted from the first injection at the times of 9.2 (*a*), 16.4 (*b*), 18.1 (*c*), 20.1 (*d*), and 33.9 (*e*) s. The phase direction is shown as a *white arrow* in **a**

the third curves should have been affected by the previous injection of Gd-DTPA.

Functional mapping images of CBF, CBV, and MTT calculated according to the theory described in the "Appendix" are shown in Fig. 6. Images obtained from this sequential assessment appeared to be reasonably clear, although slightly noisy, and were consistent among the scans. The absolute CBFs (mean ± SD) in the cortical gray matter area (mainly the parietal cortex, Pt) were 24.04 ± 2.88, 17.75 ± 3.34, and 31.87 ± 7.27 ml g^{-1} min^{-1} for the first, second, and third scans, respectively. The HT-to-Pt CBF ratios were 46.7, 51.5, and 43.0% for the first, second, and third scans, respectively. The CBVs were 0.49 (0.44), 0.50 (0.35), and 0.47 (0.41) ml/ml in the Pt (the HT) region in the first, second, and third scans, respectively. The MTTs in the same regions were 1.22 (2.51), 1.72 (2.29),

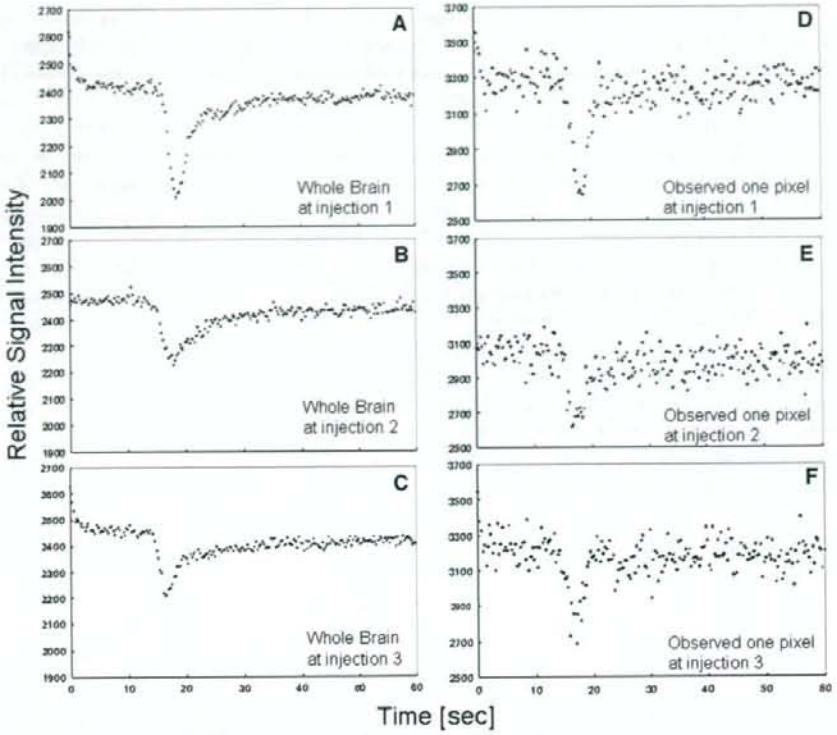

Fig. 5 TIC dynamic changes in the whole brain are shown in the first injection (**a**), the second injection (**b**), and the third injection (**c**). For each injection, a one-pixel ROI was selected and observed, as shown for the first (**d**), second (**e**) and third (**f**) injections, respectively. The negative enhancement changes in the rate from peak signal intensity to baseline were 16.8% (**a**), 10.0% (**b**), and 10.3% (**c**) at the whole brain (average 12.3, SD 3.9). The peak-to-base fractions at selected ROIs were 19.2% (**d**), 14.5% (**e**), and 16.9% (**f**) (average 16.9, SD 2.3), for the first, second, and third injections, respectively

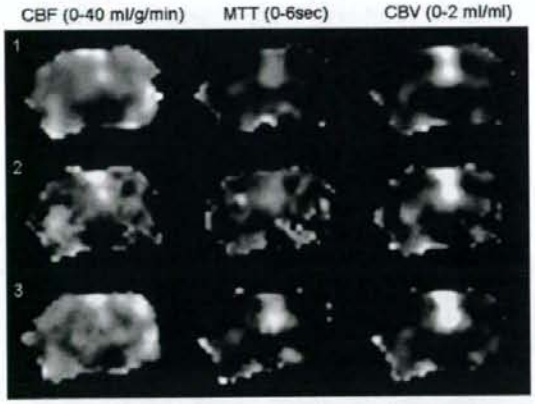

Fig. 6 *First column on the left*: CBF maps using the AIF from MCA, pictured in a grayscale from 0 to 4 ml g^{-1} min^{-1}. MTT maps are shown in the *middle column*, followed by CBV maps of 0–2 ml g^{-1} min^{-1} in the *column on the right*. Deconvolution was carried out pixel by pixel with b-SVD and then smoothed to 0.15625 × 0.15625 mm in-plane resolution from the acquired voxel resolution of 0.625 × 0.625 × 3 mm (1.17 mm^3) in DSC-MRI

and 0.92 (2.16) s in each of the three scans. Among the three injections, the absolute MTTs (mean ± SD) were 1.29 ± 0.40 s in the Pt and 2.32 ± 0.17 s in the HT region.

4 Discussion

This study demonstrated that our system of a human whole-body 3-T MRI fitted with an in-house solenoid coil developed for small animals can provide morphologic and functional images of the rat brain in vivo. The quality of T_1W and T_2W images obtained with a scan duration of approximately 10 min was better than those obtained in previous studies in which 1.5-T clinical MRI scanners [3] were employed. The neocortex and large subcortical structures, such as the Thal and HC, are readily recognized from their topographic relationship to the CC, the ventricular system, and the subarachnoid space [2]. In T_1W images, the cerebrospinal fluid (CSF)-containing spaces are visible as they are hypointense, and the arterial flow showed a signal loss caused by so-called flow void effects, which is typically seen in the spin echo sequence [2]. In T_2W images, the CSF was bright and white (prolonged T_2 relaxation time), whereas the myelinated white matter was black (short T_2 relaxation time). The white matter tracts such as the IC and CC were clearly visible in both T_1W and T_2W images, and better quality was obtained compared to previous reports employing 1.0- and 1.5-T clinical MRI scanners [2, 3].

Magnetic resonance angiography images also clearly showed the structure of the distal MCA branches. The MRA findings of interhemispheric differences with regards to MCA in the SD rat were also consistent with a previous report on Wistar rats [29], which indicated left-to-right asymmetric structure in three out of ten Wistar rats using a 7-T MRI scanner dedicated to small-animal imaging [29]. Our MRA images are superior to those obtained in previous work [11] that employed a clinical 3-T MRI scanner and that only showed the major cerebral arteries and the carotid arteries because they focused mainly on validating occlusion models [11]. The superior quality of our MRA images can largely be attributed to the type of RF coil we used. Ours is a three-turn solenoid coil that covers only the cerebral area, whereas the previous work [11] employed a single-turn coil (diameter of 6.4 cm and length of 10 cm) that covered the whole head, including the brain and the neck. Additionally, the prolonged acquisition period in our study (almost 20 min) compared to the acquisition period used in the previous study [11] (almost 4 min) may have been a factor that led to higher-quality MRA images.

An important point about this study is that DSC-MRI images of reasonable quality can also be obtained with a clinical MRI scanner at 3 T on rats. In addition, we were able to extract the AIF from the rat brain, which is an important accomplishment. Selection of an ROI in the MCA region successfully provided the AIF. Spatial distortion or susceptibility artifacts were not visible in our observations. Signal changes were obtained during DSC-MRI following a single dose of Gd-DTPA. During this study, the dedicated transmit and receive RF coils were considered to be crucial to obtaining a reasonable SNR. Our study was performed with the same sequence and the same dose rate (0.1 mmol/kg) of Gd-DTPA that are commonly used in clinical examinations. Moreover, it was performed with high ($1.17\ mm^3$)-resolution dynamic imaging.

The quantitative images of CBF were consistent with those in a previous report on the use of [^{14}C] iodoantipyrine [30]. Namely, the HT-to-Pt contrast in CBF was 43–52% in this study, which is close to the values reported by Bloom et al. [30] of 44–58%. Although the absolute CBF and CBV values in our study were different from those obtained previously [13, 30, 31], the uncertain scaling factors for each of these were canceled out when calculating the MTT with Eq. 5 [32] (see also the "Appendix"). The MTT obtained in this study was comparable to those obtained in previous work [31, 33].

We noticed that the absolute CBF and CBV values were overestimated, which suggests that some limitations apply, such as the partial volume effect (PVE) caused by insufficient spatial resolution as compared with the anatomic structure of the MCA. Detection of AIF with a repeat injection was performed (Fig. 5, right row). The major MCA diameter was approximately 0.5 mm at the maximum, as evaluated from Fig. 3, which suggested that the measured AIF is largely influenced by the PVE [24]. Also, the differences in absolute value may be due to the fact that a nonlinear relationship exists between the signal intensity and the contrast agent concentration. Previous reports have proposed nonlinearity correction methods for brain tissue [34] and AIF [35]. Further studies are needed to confirm the accuracy and the reproducibility [36]. Image distortion caused by dielectric effects [37] and/or EPI distortion [38] are other sources of error, and should be investigated systematically.

Improving the quality of the original dynamic images acquired would also improve the mapping image quality. In order to achieve better detection of the dynamic susceptibility contrast caused by T_2* signals, the optimization of TE, FA and the acquisition matrix should be investigated. We speculate that a multichannel phased array coil and parallel imaging techniques would reduce the level of distortion. The DSC-MRI in this study was obtained for only a single slice. Further careful attention is needed to perform multislice imaging in order to minimize inflow effects [35]. In our study, the contrast concentration $C(t)$ curves including the AIFs varied slightly among the three injections. A sophisticated injector system that is MR-compatible may improve the variation.

A dedicated high magnetic field scanner equipped with a dedicated small bore is the optimal device for small-animal imaging. However, such systems are not commonly available. The system developed in this study might serve as a low-cost solution or an alternative. The use of the present system provides an opportunity to use the same imaging platform available for clinical studies for small-animal imaging [7]. This would allow us to determine pathophysiological status from MRI signals using animal models with various diseases. More importantly, the optimization of several scan parameters, which has been difficult to achieve in clinical patients, can easily be performed on small animals with this system. In particular, the reproducibility of the assessment of CBF with DSC-MRI, which has been reported to be a limitation on clinical studies [19, 36], could be improved by performing a systematic evaluation of each scan parameter when this system is used on small animals rather than clinical patients. With the addition of a high-strength insert gradient coil [39], which allows for thinner slices and much faster read-out, the system performance and the spatial resolution with an acceptable SNR can be improved. The use of adapting coils could be an effective solution for those who operate MR scanners for human subjects and intend to gain experience [40] in preclinical research.

5 Conclusion

In this preclinical study on rats, reasonable image quality was obtained for T_1W, T_2W, and contrast-free TOF-MRA images generated using a human whole-body 3-T MRI scanner and a newly developed solenoid coil. In DSC-MRI, this system visualized transient signal changes with a single dose of Gd-DTPA and using the same sequences commonly used in clinical examinations. A human whole-body 3-T MRI scanner and dedicated coil make it possible to detect the AIF in the MCA region of Wistar rats. High-resolution DSC-MRI was accomplished with a clinical scanner, but the spatial resolution with an acceptable SNR was insufficient for the rat brain. Although there may be some remaining issues relating to AIF, we have shown the potential of DSC-MRI in our study.

Acknowledgments The authors would like to express our appreciation to the reviewers, the editors and the editorial assistants of *Radiological Physics and Technology* for their invaluable advice on how to improve our manuscript. This study was supported by a grant for research on Advanced Medical Technology from the Ministry of Health, Labor and Welfare, Japan. We would like to thank the VPL released by AZE Ltd. (Tokyo, Japan) and the software library provided by the Oxford University Center for Functional MRI of the Brain. We are grateful to the staff at the National Cardiovascular Center for their invaluable contributions and efforts. Last but not least, we would like to express our thanks to Miss Atra Ardekani (a summer intern from McGill University in Montreal, Quebec, Canada).

Appendix: Calculation of functional mapping images from DSC-MRI

The observed TIC $S(t)$ was converted to a time-versus-concentration curve (TCC) $C(t)$ by the following equation [16, 36]:

$$C(t) = k \cdot \Delta R2^*(t) = -k \cdot \ln(S(0)/S(t))/\mathrm{TE}, \quad (1)$$

where $\Delta R2^*$ is the change in the T_2^* relaxation rate and k is a constant. In this study, it was assumed that $k = 1$. $S(0)$ is the pre-contrast (baseline) signal and $S(t)$ is the measured signal at time t. The next step was to fit this first-pass period of TCC to a gamma variate function:

$$C(t) = a(t-b)^c \exp(-(t-b)/d), \quad (2)$$

where a, b, c, and d were determined by nonlinear least-squares fitting. To minimize the effects of the recirculation of the contrast agent, data were neglected in the fit if these concentrations were less than 50% of the maximum after the peak of the TCC.

The fitted tissue TCC $Ct(t)$ was deconvolved by the fitted AIF $C_{\mathrm{AIF}}(t)$ by using singular value decomposition with a block-circulant deconvolution matrix (b-SVD) method [28] according to the equation

$$\mathrm{CBF} \cdot R(t) = Ct(t) \otimes^{-1} C_{\mathrm{AIF}}(t), \quad (3)$$

where $\otimes^{-1}$ represents the deconvolution operator and $R(t)$ is a residue function representing the tissue response to an instantaneous bolus. CBF·$R(t)$ was estimated by deconvolving $Ct(t)$ by $C_{\mathrm{AIF}}(t)$ using b-SVD, and then CBF was determined as the maximum value of the obtained CBF·$R(t)$.

The CBV was calculated as follows:

$$\mathrm{CBV} = \int_0^\infty Ct(t)\mathrm{d}t \Big/ \int_0^\infty C_{\mathrm{AIF}}(t)\mathrm{d}t. \quad (4)$$

Lastly, the MTT is calculated from CBF and CBV by applying the central volume principle [32]:

$$\mathrm{MTT} = \mathrm{CBV}/\mathrm{CBF}. \quad (5)$$

References

1. Brockmann MA, Kemmling A, Groden C. Current issues and perspectives in small rodent magnetic resonance imaging using clinical MRI scanners. Methods. 2007;43:79–87.
2. Smith DA, Clarke LP, Fiedler JA, Murtagh FR, Bonaroti EA, Sengstock GJ, et al. Use of a clinical MR scanner for imaging the rat brain. Brain Res Bull. 1993;31(1–2):115–20.
3. Guzman R, Lövblad KO, Meyer M, Spenger C, Schroth G, Widmer HR. Imaging the rat brain on a 1.5 T clinical MR-scanner. J Neurosci Methods. 2000;97(1):77–85.
4. Fujioka M, Taoka T, Matsuo Y, Hiramatsu KI, Sakaki T. Novel brain ischemic change on MRI: delayed ischemic hyperintensity on T_1-weighted images and selective neuronal death in the caudoputamen of rats after brief focal ischemia. Stroke. 1999;30(5):1043–6.
5. Thorsen F, Ersland L, Nordli H, Enger PO, Huszthy PC, Lundervold A, et al. Imaging of experimental rat gliomas using a clinical MR scanner. J Neurooncol. 2003;63(3):225–31.
6. Biswas J, Nelson CB, Runge VM, Wintersperger BJ, Baumann SS, Jackson CB, et al. Brain tumor enhancement in magnetic resonance iimaging: comparison of signal-to-noise ratio (SNR) and contrast-to-noise ratio (CNR) at 1.5 versus 3 Tesla. Invest Radiol. 2005;40:792–7.
7. Shimamura M, Sato N, Sata M, Kurinami H, Takeuchi D, Wakayama K, et al. Delayed postischemic treatment with fluvastatin improved cognitive impairment after stroke in rats. Stroke. 2007;38:3251–8.
8. Lee JM, Zhai G, Liu Q, Gonzales ER, Yin K, Yan P, et al. Vascular permeability precedes spontaneous intracerebral hemorrhage in stroke-prone spontaneously hypertensive rats. Stroke. 2007;38:3289–91.
9. Wintersperger BJ, Runge VM, Biswas J, Reiser MF, Schoenberg SO. Brain tumor enhancement in mr imaging at 3 Tesla: comparison of SNR and CNR gain using TSE and GRE techniques. Invest Radiol. 2007;42:558–63.
10. Sato H, Enmi J, Teramoto N, Hayashi T, Yamamoto A, Tsuji T, et al. Comparison of Gd-DTPA-induced signal enhancements in rat brain C6 glioma among different pulse sequences in 3-Tesla magnetic resonance imaging. Acta Radiol. 2008;49:172–9.
11. Yang YM, Feng X, Yao ZW, Tang WJ, Liu HQ, Zhang L. Magnetic resonance angiography of carotid and cerebral arterial

occlusion in rats using a clinical scanner. J Neurosci Methods. 2008;167(2):176–83.
12. Rosen BR, Belliveau JW, Vevea JM, Brady TJ. Perfusion imaging with NMR contrast agents. Magn Reson Med. 1990;14(2):249–65.
13. Calamante F, Thomas DL, Pell GS, Wiersma J, Turner R. Measuring cerebral blood flow using magnetic resonance imaging techniques. J Cereb Blood Flow Metab. 1999;19(7):701–35.
14. Yamada K, Wu O, Gonzalez RG, Bakker D, Østergaard L, Copen WA, et al. Magnetic resonance perfusion-weighted imaging of acute cerebral infarction: effect of the calculation methods and underlying vasculopathy. Stroke. 2002;33(1):87–94.
15. Tamura H, Hatazawa J, Toyoshima H, Shimosegawa E, Okudera T. Detection of deoxygenation-related signal change in acute Ischemic stroke patients by T2*-weighted magnetic resonance imaging. Stroke. 2002;33(4):967–71.
16. Calamante F, Gadian DG, Connelly A. Quantification of perfusion using bolus tracking magnetic resonance imaging in stroke: assumptions, limitations, and potential implications for clinical use. Stroke. 2002;33(4):1146–51.
17. Latchaw RE, Yonas H, Hunter GJ, Yuh WT, Ueda T, Sorensen AG, et al. Guidelines and recommendations for perfusion imaging in cerebral ischemia: a scientific statement for healthcare professionals by the Writing Group on Perfusion Imaging, from the Council on Cardiovascular Radiology of the American Heart Association. Stroke. 2003;34(4):1084–104.
18. Carroll TJ, Rowley HA, Haughton VM. Automatic calculation of the arterial input function for cerebral perfusion imaging with MR imaging. Radiology. 2003;227(2):593–600.
19. Wintermark M, Sesay M, Barbier E, Borbély K, Dillon WP, Eastwood JD, et al. Comparative overview of brain perfusion imaging techniques. Stroke. 2005;36(9):83–99.
20. Bruening R, Kwong KK, Vevea MJ, Hochberg FH, Cher L, Harsh GR 4th, et al. Echo-planar MR determination of relative cerebral blood volume in human brain tumors: T1 versus T2 weighting. AJNR Am J Neuroradiol. 1996;17(5):831–40.
21. Chen F, Suzuki Y, Nagai N, Peeters R, Coenegrachts K, Coudyzer W, et al. Visualization of stroke with clinical MR imagers in rats: a feasibility study. Radiology. 2004;233:905–11.
22. Chen F, Suzuki Y, Nagai N, Sun X, Coudyzer W, Yu J, et al. Delayed perfusion phenomenon in a rat stroke model at 1.5 T MR: An imaging sign parallel to spontaneous reperfusion and ischemic penumbra? Eur J Radiol. 2007;61:70–8.
23. Fan G, Zang P, Jing F, Wu Z, Guo Q. Usefulness of diffusion/perfusion-weighted MRI in rat gliomas: correlation with histopathology. Acad Radiol. 2005;12(5):640–51.
24. van Osch MJ, van der Grond J, Bakker CJ. Partial volume effects on arterial input functions: shape and amplitude distortions and their correction. J Magn Reson Imaging. 2005;22(6):704–9.
25. Wada Y, Hara T, Miyati T. Basic assessment of the CNR measurement method of MRI system in phantom—suggestion for improvement in the CNR evaluation method. Nippon Hoshasen Gijutsu Gakkai Zasshi. 2008;64(2):268–76.
26. Ogura A, Maeda F, Miyai A, Hongoh T. Accuracy of contrast-to-noise ratio measurement for magnetic resonance clinical images. Nippon Hoshasen Gijutsu Gakkai Zasshi. 2004;60(11):1543–9.
27. Miyati T. Image quality assessment in magnetic resonance imaging. Nippon Hoshasen Gijutsu Gakkai Zasshi. 2002;58(1):40–8.
28. Wu O, Ostergaard L, Weisskoff RM, Benner T, Rosen BR, Sorensen AG. Tracer arrival timing-insensitive technique for estimating flow in MR perfusion-weighted imaging using singular value decomposition with a block-circulant deconvolution matrix. Magn Reson Med. 2003;50:164–74.
29. Besselmann M, Liu M, Diedenhofen M, Franke C, Hoehn M. MR angiographic investigation of transient focal cerebral ischemia in rat. NMR Biomed. 2001;14(5):289–96.
30. Bloom AS, Tershner S, Fuller SA, Stein EA. Cannabinoid-induced alterations in regional cerebral blood flow in the rat. Pharmacol Biochem Behav. 1997;57(4):625–31.
31. Shockley RP, LaManna JC. Determination of rat cerebral cortical blood volume changes by capillary mean transit time analysis during hypoxia, hypercapnia and hyperventilation. Brain Res. 1998;454(1–2):170–8.
32. Meier P, Zierler KL. On the theory of the indicator-dilution method for measurement of blood flow and volume. J Appl Physiol. 1954;6:731–44.
33. Johansson E, Månsson S, Wirestam R, Svensson J, Petersson JS, Golman K, et al. Cerebral perfusion assessment by bolus tracking using hyperpolarized 13C. Magn Reson Med. 2004;51(3):464–72.
34. Enmi J, Hayashi T, Watabe H, Moriwaki H, Yamada N, Iida H. Measurement of cerebral blood flow with dynamic susceptibility contrast MRI and comparison with O-15 positron emission tomography. Int Congr Ser. 2004;1265:150–8.
35. Calamante F, Vonken EJ, van Osch MJ. Contrast agent concentration measurements affecting quantification of bolus-tracking perfusion MRI. Magn Reson Med. 2007;58:544–53.
36. Grandin CB, Bol A, Smith AM, Michel C, Cosnard G. Absolute CBF and CBV measurements by MRI bolus tracking before and after acetazolamide challenge: repeatability and comparison with PET in humans. Neuroimage. 2005;26:525–35.
37. Kuhl CK, Träber F, Schild HH. Whole-body high-field-strength (3.0-T) MR imaging in clinical practice. Part I. Technical considerations and clinical applications. Radiology. 2008;246(3):675–96.
38. Jezzard P, Clare S. Sources of distortion in functional MRI data. Hum Brain Mapp. 1999;8(2–3):80–5.
39. Mayer D, Zahr NM, Adalsteinsson E, Rutt B, Sullivan EV, Pfefferbaum A. In vivo fiber tracking in the rat brain on a clinical 3T MRI system using a high strength insert gradient coil. Neuroimage. 2007;35(3):1077–85.
40. Graf H, Martirosian P, Schick F, Grieser M, Bellemann ME. Inductively coupled rf coils for examinations of small animals and objects in standard whole-body MR scanners. Med Phys. 2003;30(6):1241–5.

Eur J Nucl Med Mol Imaging
DOI 10.1007/s00259-007-0654-4

ORIGINAL ARTICLE

Absolute quantitation of myocardial blood flow with ^{201}Tl and dynamic SPECT in canine: optimisation and validation of kinetic modelling

Hidehiro Iida · Stefan Eberl · Kyeong-Min Kim · Yoshikazu Tamura · Yukihiko Ono · Mayumi Nakazawa · Antti Sohlberg · Tsutomu Zeniya · Takuya Hayashi · Hiroshi Watabe

Received: 18 September 2007 / Accepted: 4 November 2007

Abstract
Purpose ^{201}Tl has been extensively used for myocardial perfusion and viability assessment. Unlike ^{99m}Tc-labelled agents, such as ^{99m}Tc-sestamibi and ^{99m}Tc-tetrofosmine, the regional concentration of ^{201}Tl varies with time. This study is intended to validate a kinetic modelling approach for in vivo quantitative estimation of regional myocardial blood flow (MBF) and volume of distribution of ^{201}Tl using dynamic SPECT.
Methods Dynamic SPECT was carried out on 20 normal canines after the intravenous administration of ^{201}Tl using a commercial SPECT system. Seven animals were studied at rest, nine during adenosine infusion, and four after beta-blocker administration. Quantitative images were reconstructed with a previously validated technique, employing OS-EM with attenuation-correction, and transmission-dependent convolution subtraction scatter correction. Measured regional time–activity curves in myocardial segments were fitted to two- and three-compartment models. Regional MBF was defined as the influx rate constant (K_1) with corrections for the partial volume effect, haematocrit and limited first-pass extraction fraction, and was compared with that determined from radio-labelled microspheres experiments.
Results Regional time–activity curves responded well to pharmacological stress. Quantitative MBF values were higher with adenosine and decreased after beta-blocker compared to a resting condition. MBFs obtained with SPECT (MBF_{SPECT}) correlated well with the MBF values obtained by the radio-labelled microspheres (MBF_{MS}) ($MBF_{SPECT}=-0.067+1.042\times MBF_{MS}$, $p<0.001$). The three-compartment model provided better fit than the two-compartment model, but the difference in MBF values between the two methods was small and could be accounted for with a simple linear regression.
Conclusion Absolute quantitation of regional MBF, for a wide physiological flow range, appears to be feasible using ^{201}Tl and dynamic SPECT.

Keywords Myocardial blood flow · Dynamic SPECT · Thallium-201 · Compartment model · Quantitation

H. Iida (✉) · S. Eberl · K.-M. Kim · M. Nakazawa · A. Sohlberg · T. Zeniya · T. Hayashi · H. Watabe
Department of Investigative Radiology,
National Cardiovascular Center Research Institute,
Fujishiro-dai,
Suita City, Osaka 565-8565, Japan
e-mail: iida@ri.ncvc.go.jp

S. Eberl
PET and Nuclear Medicine Department,
Royal Prince Alfred Hospital,
Missenden Road,
Camperdown, NSW 2050, Australia

Y. Tamura
Department of Cardiology, Akita Kumiai General Hospital,
1-1-1, Nishi-bukuro, Iijima,
Akita City 011-0948, Japan

Y. Ono
Akita Research Institute of Brain,
6-10, Senshu-Kubota Machi,
Akita City 010-0874, Japan

Introduction

Myocardial perfusion imaging using Thallium-201 (^{201}Tl) is well established in routine clinical practice for detecting

exercise-induced myocardial ischaemia and/or for assessing myocardial viability in patients with coronary artery disease. The diagnosis, however, has been limited to qualitative or visual assessment of the physical extent of the defect areas rather than quantitative assessment of physiological functions. Quantitative methods would for example enable longitudinal studies when assessing therapy response and pharmacological interventions. Some groups have already investigated the feasibility of estimating quantitative parameters with dynamic SPECT in the myocardium using ^{201}Tl [1] and ^{99m}Tc-Teboroxime [1, 2], but these techniques have not yet been applied to clinical practice. This is largely attributed to the fact that quantitative reconstruction programmes are not readily available on commercial SPECT systems.

We have developed a reconstruction programme package for SPECT, which can accurately provide quantitative images of radio-labelled tracer distributions in vivo, which is a pre-requisite for absolute physiological parameter estimation. The adequacy and accuracy of these methods have been demonstrated in multiple papers for ^{99m}Tc and ^{201}Tl in cardiac studies [3–5], and for ^{99m}Tc and ^{123}I in brain studies [6]. It has also been demonstrated, in brain studies, that physiological parameters such as cerebral perfusion [6] and cerebral flow reactivity [7] obtained using our package were as accurate as those determined by PET. These findings suggest that absolute quantitation of regional myocardial perfusion might also be possible in a clinical setting using commercial SPECT cameras.

^{201}Tl is a potassium analogue, and its kinetics has been extensively investigated in previous studies [8, 9]. Due to the high first-pass extraction fraction (EF) [10] and a large distribution volume, ^{201}Tl has been considered an ideal tracer for quantitation of absolute myocardial blood flow, not only at rest but also at hyperemic conditions. As a clinical implication, quantitative assessment of MBF and coronary flow reserve is important. For instance, coronary microvascular dysfunction or impaired endothelial function in patients with coronary risk factors or patients with cardiomyopathy or with heart failure is an un-resolved important issue to answer [11]. Coronary flow reserve can also be reduced in patients with hyper-cholesterolemia without overt coronary stenosis [12]. The low energy and long half-life of ^{201}Tl have, however, seriously limited its use in nuclear cardiology.

The goal of this study was to validate our reconstruction methodology for the estimation of myocardial blood flow using ^{201}Tl and dynamic SPECT using tissue time–activity curves (TTAC) derived from myocardial regions. In addition, we aimed to find the optimal kinetic model configuration and to investigate the factors affecting the estimation of physiological parameters such as the partial volume effect (PVE), appropriate choice of input function, conversion from plasma to blood flow using haematocrit (Hct) and the limited first-pass tracer EF.

Materials and methods

Subjects

A total of 21 dogs were studied in which 8 were in a resting condition, 9 dogs during constant infusion of adenosine for increased MBF, and 4 dogs during constant infusion of beta-blocker. Of the 21 studies, 1 study was un-successful and projection data could not be retrieved from the scanner, reducing the number of resting studies to 7 and total dog studies to 20. Adenosine was infused continuously over the study duration at a rate ranging from 140 to 700 mg/kg/h to achieve a range of blood flow increases. An initial dose of beta-blockers ranging from 2 to 6 mg was given, followed by a constant infusion for the duration of the study of 2 or 4 mg/h. The study protocol was approved by the animal ethics committee at the Akita Research Institute of Brain, Akita City, Japan where all experiments were carried out.

SPECT procedures

All dogs were anaesthetised, and the catheters for dose administration and arterial blood sampling were inserted before the study. The SPECT system was a conventional dual-head gamma camera (Toshiba GCA-7200A, Tokyo, Japan) fitted with short focal length fan-beam collimators (LEHR-Fan). The transverse field-of-view (FOV) was 22 cm diameter and axial FOV was 20 cm. The dogs were carefully taped into a cradle to minimise motion during the study, and also to ensure that no truncation occurred. Heart rate and blood pressure were monitored throughout the study and recorded at regular intervals.

Before the injection of any tracer, a 15-min transmission study was carried out in which a rod source filled with approximately 740 MBq of ^{99m}Tc was placed along the focal line of one of the fan-beam collimators (see Fig. 1). The transmission study was followed by injection of 3 MBq of ^{141}Ce microspheres into the left ventricle via a catheter and blood was withdrawn from the aorta at a constant flow rate of 5 ml/min for 2 min to serve as an input function. For the pharmacological intervention studies, adenosine infusion or beta-blocker injection followed by infusion was commenced before the ^{141}Ce microsphere administration.

Dynamic SPECT was commenced with the start of the 4-min constant infusion of 110 MBq ^{201}Tl. The frame collection rates and 360° rotation times were 10×1 min (rotation time 15 s), 6×2 min (30 s), 3×4 min (60 s) and 5×5 min (60 s) for the first hour for all studies. Resting blood flow studies had an additional 18×10 min (120 s) frames collected for a total study period over 4 h. The shorter total study time for the drug infusion studies was mandated by the difficulties in keeping the dogs stable with prolonged infusions of the drugs used. A 34% energy

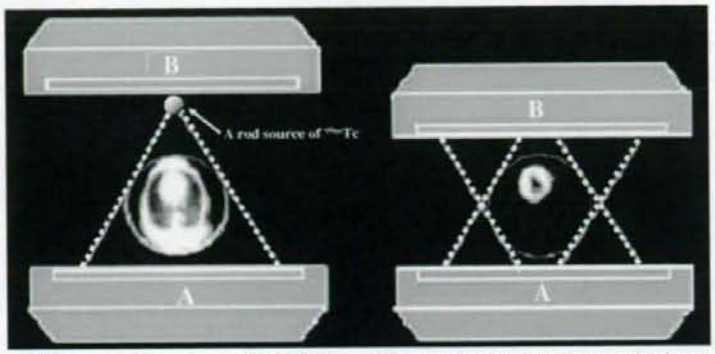

Fig. 1 Schematic diagram of data acquisition using a clinical dual-headed SPECT camera fitted with fan-beam collimators. Transmission scan was performed using a ^{99m}Tc-filled rod source placed at a focal line of one of the collimators, and only one of the detectors was used (*left*). Both detectors were used in the emission scan (*right*)

window centred on 77 keV was used for the ^{201}Tl acquisitions [4, 13].

Arterial blood samples were taken every 20 s for the first 6 min, every 60 s for 6–10 min, 120 s for 10–20 min, 300 s for 20–30 min and 600 s for 30–60 min. For the resting studies, blood samples were also taken every 20 min for 1–2 h and additional samples at 2.5, 3 and 4 h post-^{201}Tl infusion. In six studies, plasma was separated immediately after sampling by centrifugation, and plasma samples were counted in a well counter cross-calibrated with the SPECT scanner. To minimise the effects of the continued exchange of ^{201}Tl between plasma and red blood cells in the test tubes after sampling, immediate, rapid separation of plasma from whole blood was required. An averaged relationship between plasma and whole blood concentration ratio over time was obtained, and then multiplied with the whole blood curves for all studies to derive a plasma input function.

At the end of the SPECT study, the microsphere blood flow measurement was repeated with ^{51}Cr microspheres. The dogs were then killed by injection of potassium chloride (KCl) and the myocardium was dissected into samples suitable for counting in the well counter. The ^{201}Tl concentration in the tissue samples was derived from the sample weight normalised gamma counter counts. The samples were stored to allow for the decay of ^{201}Tl ($T_{1/2}$= 73 h vs $T_{1/2}$=32.5 days for ^{141}Ce and 27.8 days for ^{51}Cr) and then counted to measure the ^{141}Ce and ^{51}Cr activities. Separation between ^{141}Ce and ^{51}Cr counts was based on their respective gamma ray energies (145 keV for ^{141}Ce and 323 keV for ^{51}Cr).

SPECT data processing

Projection data were processed according to previously described procedures [5]. Briefly, the transmission data obtained by the fan-beam collimator were first re-binned into parallel projections. Transmission projections were normalised by blank projection, re-constructed to generate quantitative maps of the attenuation coefficient for ^{99m}Tc and then linearly scaled to provide attenuation correction maps for ^{201}Tl. Emission data were corrected for detector non-uniformity and also re-binned into parallel projections. The projection data were then corrected for scatter with transmission-dependent convolution subtraction (TDCS) originally proposed by Meikle et al. [14] and further optimised by our group [4, 5]. The emission projection data were re-constructed with the OS-EM reconstruction algorithm [15] using three iterations and ten subsets. The re-constructed images were cross-calibrated with the well counter system.

Data analysis

Re-constructed images were normalised by acquisition time for each frame. Multiple circular regions of interest (ROI) were drawn on the myocardium, and the TTAC of ^{201}Tl were generated for the anterior, apical, lateral, posterior and septal areas of the myocardium. The two-compartment model (one tissue compartment) and three-compartment model (two tissue compartments) shown in Fig. 2 were applied to determine two parameters (K_1 and K_2) for the two-compartment model and four parameters (K_1–K_4) for the three-compartment model by means of non-linear least squares fitting (NLLSF).

The regional MBF was considered to be related to K_1 obtained from compartment model fits. K_1 is, however, affected by the PVE, Hct and the limited first-pass EF whose effects were corrected according to Eq. 1:

$$\mathrm{MBF} = \frac{\mathrm{PVE}}{\mathrm{EF} \times (1 - \mathrm{Hct})} \times K_1 \quad (1)$$

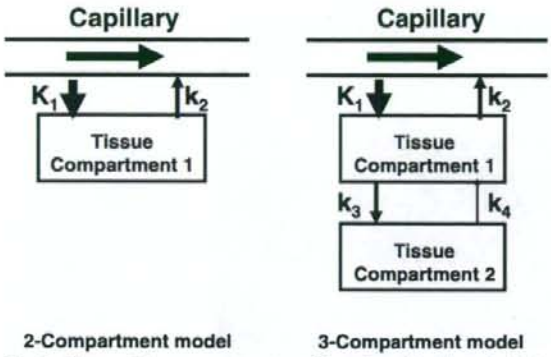

Fig. 2 Two- and three-compartment models evaluated in this study. K_1 in units of ml/min/g denotes the regional MBF for both models. Distribution volume (V_d) in units of ml/g is defined as K_1/K_2 for the two-compartment mode, and $\frac{K_1}{k_2}\left(1+\frac{k_3}{k_4}\right)$ for the three-compartment model

The physiological basis for the correction factors in Eq. 1 can be described as follows:

1. TTACs obtained from SPECT images are under-estimated due to the limited spatial resolution relative to the myocardial wall thickness and also due the myocardial contractile motion. This phenomenon is known as PVE. The PVE correction factor for each TTAC was determined from the ratio of the last SPECT frame counts to the ^{201}Tl myocardial tissue sample counts obtained from the tissue samples taken and measured with the well counter at the end of the SPECT scan.
2. The arterial input function for the compartment model studies was defined from the plasma radioactivity concentration curve, rather than the whole blood radioactivity curve. K_1 is therefore the regional "plasma" flow. Thus, for comparison with the microsphere flow measurements, which estimates the whole blood flow, K_1 was divided by (1−Hct) to obtain the flow for the total blood.
3. For a tracer with limited first-pass EF<1.0, flow (MBF) is related to K_1 by K_1=EF×MBF. The first-pass EF is flow-dependent and decreases at high flow. We have applied an empirical formulation for the first-pass EF based on the data by Weich et al. [10] (EF=0.84−0.524·$\log_{10}(K_1^*)$ where K_1^* is $K_1/(1-\text{Hct})$. The K_1 values obtained with two- and three-compartment models with/without corrections according to Eq. 1 were compared to the average of microsphere blood flow values obtained pre- and post-dynamic SPECT scan.

The distribution volume of ^{201}Tl (V_d) was defined as

$$V_d = \frac{K_1}{k_2} \text{ for the two} - \text{compartment model} \quad (2a)$$

$$V_d = \frac{K_1}{K_2}\left(1+\frac{K_3}{K_4}\right) \text{ for the three} - \text{compartment model.} \quad (2b)$$

As mentioned before, the resting studies were collected for 4 h, whilst the adenosine and beta-blocker studies were collected for approximately 1 h. To investigate whether the shorter collection time introduces systematic bias, NLLSF fits restricted to the first 1 h of the resting study data were also performed and compared with the V_d values from the full 4 h resting data set and with the estimates obtained from the beta-blocker and adenosine studies.

Akaike information criterion (AIC) and Schwarz criterion (SC) were calculated for both two-compartment and three-compartment model fits [16] to test the adequacy of the two models. All data are presented as mean±1 SD. Student's t test was employed in the comparison of the V_d values. Pearson's regression analysis was applied to compare K_1 and microsphere flow values. A probability value of <0.05 was considered statistically significant.

Results

Figure 3 shows the plasma to whole blood concentration ratios in the six dogs with rapid plasma separation and the averaged data. Equilibrium is reached after about 40 min, at which time the mean ratio was found to be 0.76. As expected, relative plasma concentration is highest early on as the tracer is injected into the plasma (and not red blood cells). ^{201}Tl is rapidly cleared from the plasma causing a rapid decline in relative plasma concentration and "undershoot" before equilibrium is established. Samples left for a prolonged period before plasma separation showed the value of approximately 0.78, which was close to the plasma to whole blood concentrations ratio at the equilibrium shown in

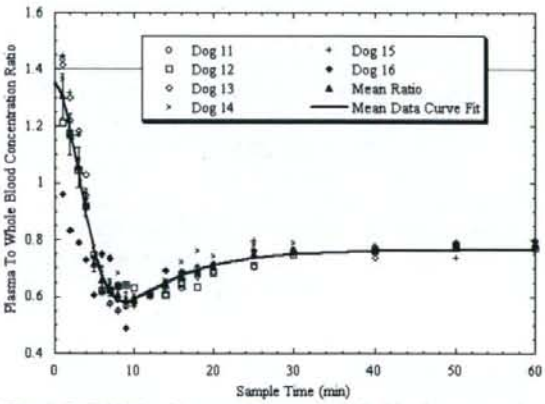

Fig. 3 Individual and mean plasma to whole blood concentration ratios over time for the six dogs with rapid plasma separation. *Error bars* indicate the standard error of the mean. *Solid line* is the curve fit to mean ratio data

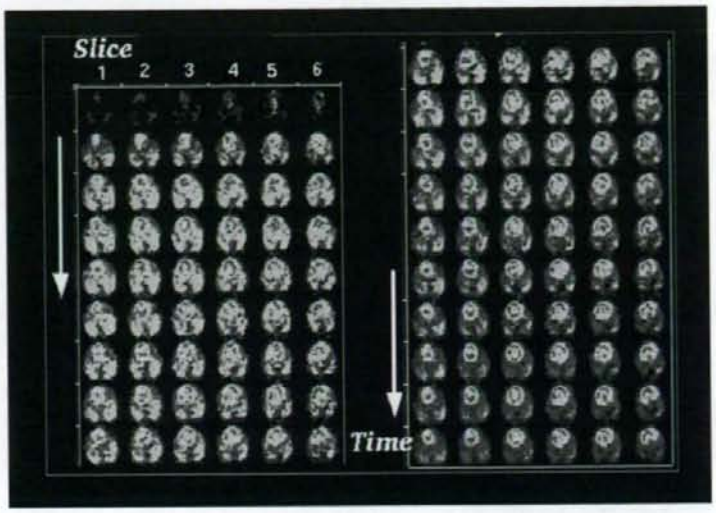

Fig. 4 A typical example of sequential SPECT images of the myocardium for six representative slices after intravenous injection of ^{201}Tl into a canine at rest

Fig. 3. The plasma to whole blood ratio curves could be approximated by the following equation:

$$R_{\mathrm{pl/wb}} = A_0 e^{-\lambda(t+\Delta t)^2} + A_1\left(1 - e^{-\lambda_2(t+\Delta t)}\right), \quad (3)$$

which resulted in A_0=1.303±0.045, A_1=0.7649±0.0056, λ_1=0.03636±0.0039 min^{-1}, λ_2=0.1263±0.0077 min^{-1} and Δt=0.9516±0.41 min. The correlation coefficient for the fit was r=0.995.

Figure 4 shows a typical example of sequential images after the intravenous injection of ^{201}Tl for six representative slices of a dog studied at rest. It can be seen that ^{201}Tl appeared in the ventricular chambers first and then gradually accumulated homogeneously into the left myocardium. The quality of these images is reasonably good, indicating that our approach of estimating the kinetic parameters by NLLSF is feasible without excessive noise

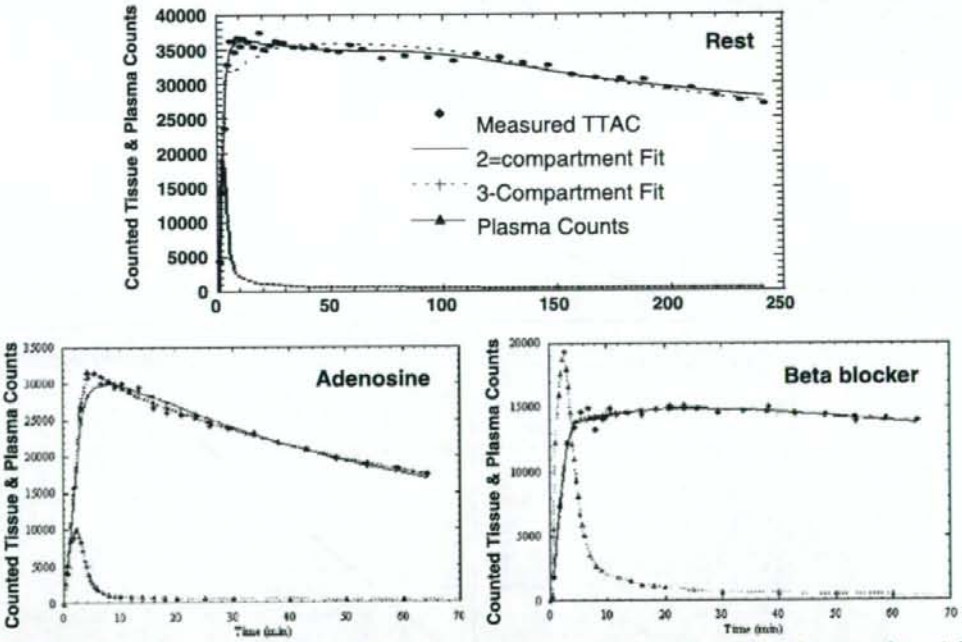

Fig. 5 TTACs and two- and three-compartment model fits for a resting, adenosine (increased MBF) and beta-blocker (reduced MBF) study. Note the different time scales for the resting study because resting studies were collected for 4 h compared to ≈1 h for the pharmacological intervention studies

amplification. Curve fits to representative TTACs for resting, beta-blocker and adenosine infusion studies are shown in Fig. 5. The height of the TTACs relative to the input function corresponded well with the pharmacological challenges. Compared to the resting studies, peaks of TTACs relative to the arterial input function were higher for adenosine and lower after beta-blocker administration. Results of kinetic fitting by the two- and three-compartment models are also plotted on this figure. Visually, the three-compartment model provided better fits than the two-compartment model to the observed TTACs, which is particularly evident for the initial scan period of the resting and adenosine studies.

Shown in Fig. 6a–e is the comparisons of K_1 obtained by NLLSF (three-compartment model fit) with the microsphere flow estimates. Values were averaged over the myocardial segments in both axes, thus each point corresponds to a single study. There was good correlation between K_1 and the microsphere flow when no corrections were applied, but K_1 significantly under-estimated the true flow (Fig. 6a). All the corrections improved the K_1 estimates (Fig. 6b–d) and the best agreement between K_1 and microsphere flow was observed when all three factors were corrected as described in Eq. 1 (Fig. 6e). Results of the regression analysis also demonstrated the highest correlation coefficient when all three correction factors were applied. Table 1 summarises the results of the Akaike information criteria (AIC) and Schwartz criteria (SC) obtained from the kinetic fitting analysis for all myocardial segments of all subjects. Both

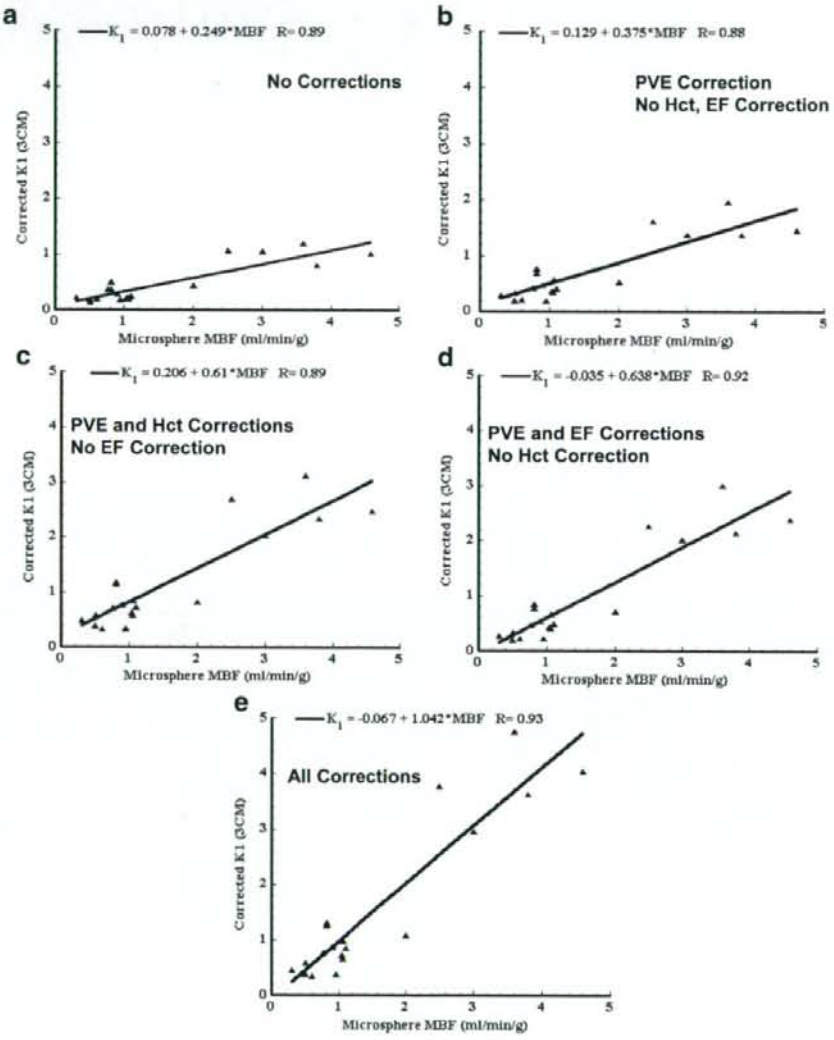

Fig. 6 Plot of K_1 derived from the three-compartment model fit against the mean of the pre- and post-dynamic SPECT microsphere blood flow measurements. **a** No correction for PVE, limited first-pass EF or conversion from plasma to blood flow has been applied. **b** Correction for PVE has been applied, but not for Hct or limited first-pass EF. **c** Corrections for PVE and Hct have been applied, but not for limited first-pass EF. **d** Corrections for PVE and limited first-pass EF have been applied, but not for Hct. **e** All corrections are applied for PVE, limited first-pass EF and Hct

Table 1 Summary of improvement in fit with the three-compartment model over the two-compartment model

Study group	Number of curves	Mean AIC two-compartment	Mean AIC three-compartment	Mean SC two-compartment	Mean SC three-compartment	Number of curves (%) (three-compartment better than two-compartment)[a]
Resting	35	652.4	630.2 ($p<0.01$)	663.8	638.4 ($p<0.01$)	24 (69)
Beta-blocker	20	378.4	378.8 (p=n.s.)	382.0 ($p<0.01$)	384.7	3 (15)
Adenosine	45	405.1	393.6 ($p<0.01$)	408.7	399.5 ($p<0.01$)	28 (62)

The p value indicates that the value in the cell is significantly lower than the corresponding other value.
AIC: Akaike information criterion, *SC*: Schwarz criterion
[a] This column gives the number of TTAC fits where the three-compartment model fit provided a significant improvement over the two-compartment fit according to all criteria (AIC, SC).

AIC and SC demonstrated that the three-compartment model fit provided significant improvement over the two-compartment model fit for resting and adenosine studies. For the beta-blocker studies, AIC between the two model fits was not significantly different, whilst SC demonstrated significantly better fit with the two-compartment model. Improved AIC and SC for the three-compartment model fit were observed in 69% of resting TTACs and 62% of adenosine TTACs, but only 15% in beta-blocker TTACs.

As shown in Fig. 7a and b, the K_1 and V_d values derived from the two-compartment model fit showed significant differences compared with those by the three-compartment model. Both K_1 and V_d were under-estimated with the two-compartment model fit compared with the three-compartment model fit. It should, however, be noted that there was a good correlation between the two- and three-compartment models for K_1, thus the bias introduced by the two-compartment model fit can potentially be corrected. K_1 values by the three-compartment model fit with all three corrections were 0.86± 0.36, 2.71±1.64 and 0.55±0.24 ml/min/g corresponding to rest, adenosine infusion (with constant infusion at 140–700 mg/kg/h) and beta-blocker (with 2–6 mg administration), respectively. Difference in V_d was less than 10% and again this bias can potentially be corrected by the regression equation. The K_1 obtained with the two-compartment model also demonstrated a good correlation with the microsphere flow (Fig. 7c), though there was again a systematic under-estimation in K_1.

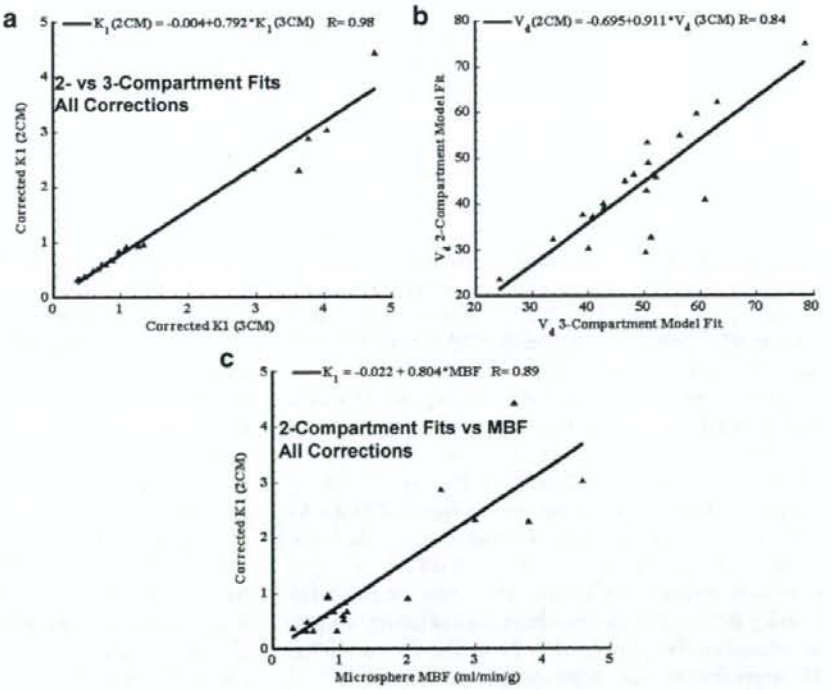

Fig. 7 **a** Plot of K_1 estimates derived from the two-compartment model fit against those from the three-compartment model fit. **b** Plot of V_d estimates derived from the two-compartment model fit against those from the three-compartment model fit. **c** Plot of K_1 values derived from the two-compartment model fit against mean of the pre- and post-dynamic SPECT microsphere blood flow measurements

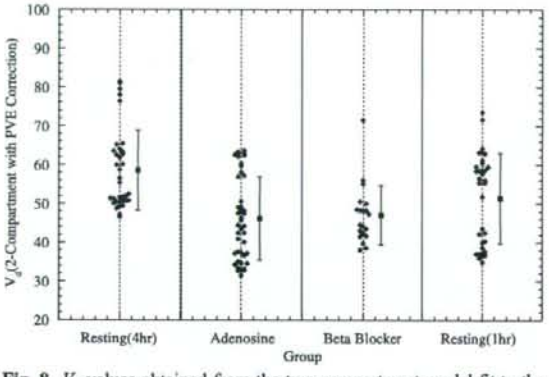

Fig. 8 V_d values obtained from the two-compartment model fit to the full 4 h resting data, adenosine and beta-blocker infusion 1 h curves and fit to first 1 h only of the resting study curves. Data from the multiple individual myocardial regions are shown

Figure 8 plots the V_d values for all evaluated myocardial segments for the fit to 4 h resting data, adenosine and beta-blocker infusion 1 h data and fit to only the first 1 h of resting data. The 4-h resting V_d values are significantly higher ($p<0.01$) compared with the adenosine, beta-blocker values and compared with the fit to the first 1 h resting data. However, the 1-h resting values are not significantly different from the beta-blocker V_d values nor the adenosine values.

Discussion

This study demonstrates that the kinetic analysis of quantitatively assessed myocardial ^{201}Tl accumulation (build-up and washout in healthy canines) provided quantitative MBF values, which agreed well with flows obtained using microspheres for a wide physiological range of flows. The size of the TTACs relative to the arterial plasma concentration corresponded well to the pharmacological stresses induced by adenosine and beta-blocker challenges. The compartmental model approach could reproduce these TTACs to make the determination of kinetic parameters, such as K_1 and V_d, possible. The three-compartment model gave results which were generally higher than the two-compartment model and which were statistically significantly better in terms of AIC, SC for the resting and adenosine studies, and this was in line with the visual inspection of the TTAC model fit curves. It should, however, be noted that the differences were only small between the two- and three-compartment model approaches, approximately 20% for K_1 and 10% for V_d The bias associated with the two-compartment model could be corrected by a linear regression as shown in Fig. 7a–c. This opens the possibility of using the more reliable two-compartment model fit due to its reduced number of parameters for routine clinical studies. The improved reliability of the two-compartment model fit in the clinical setting is particularly important if one intends to shorten the study time or generate parametric images.

The three corrections for PVE, Hct and first-pass EF proved to be important. The PVE correction method used in this work cannot, however, be applied to clinical studies, and the PVE correction in the beating heart still remains a considerable challenge in clinical studies. PVE may be reduced by gating the data, which may not, however, be feasible for the already noisy and large dynamic SPECT data sets. PVE may also be reduced by including resolution recovery as part of the reconstruction process [17–20]. Alternatively, it may also be possible to include PVE as part of the kinetic model fitting [21–25]. However, this adds extra fitting parameters and requires some parameters to be assumed fixed.

The input function is an important component in compartment model fitting. In this study, rapid arterial blood sampling was performed, and the plasma was separated by centrifugation. A number of important insights were gained by performing rapid separation of plasma in a subset of samples and dogs. It was found that ^{201}Tl enters the red blood cells as observed from the rapid separation of plasma in a subset of samples and dogs, which is not un-expected as potassium is also known [22] to be taken up by the red blood cells. The exchange of ^{201}Tl between red blood cells and plasma is relatively slow compared to the passage of blood through the capillary bed and hence direct uptake of activity from the red blood cells into tissue is believed to be negligible. Hence, tissue uptake will be dominated by the activity in the plasma during passage through the capillary bed and plasma in the substrate being measured. As a consequence, the flow measurement obtained with ^{201}Tl is plasma flow, which is in contrast to the microsphere studies, which measure whole blood flow. Conversion of plasma to blood flow was achieved by dividing the plasma flow by (1−Hct), as shown in Eq. 1, which then allowed the direct comparison with the microsphere measurements.

Rigorous estimation of the input function requires frequent arterial blood sampling. This is not only considered invasive, but also labor intensive. In addition, it has been shown in this study that rapid separation of the plasma for at least the first 30–40 min post-^{201}Tl administration is required to obtain accurate plasma concentration. If the separation of plasma is delayed, then the true plasma concentration at the time of sampling cannot be measured, which results in biased K_1 estimates. An empirical relationship of plasma to whole blood ratio as a function of time was developed and was found to be sufficiently consistent between dogs (Fig. 3) to allow the mean curve to be applied with minimal bias. Thus, in clinical practice, whole blood samples may be counted and converted to plasma concentration using the empirical relationship. This also potentially allows the input function to be obtained

non-invasively from the SPECT data using, for example, a curve derived from a left ventricular region. However, it should be noted that the relationship between plasma and whole blood counts in this study was derived for a 4-min infusion protocol and may be different for other injection protocols, such as bolus injection. Previously, it has been shown that population-based input functions calibrated with one or two blood samples could avoid the need for frequent arterial blood samples [26–28]. There is also a potential for applying this approach to ^{201}Tl studies. This is beyond the scope of this study and a systematic study should be designed to confirm this in clinical settings.

^{201}Tl has a high trans-capillary EF and thus the initial regional uptake of this tracer predominantly reflects the regional blood flow [10]. Use of a tracer that has a high first-pass EF is essential when one intends to quantitatively assess MBF at a high flow range or the coronary flow reserve. The EF of ^{201}Tl is reported as >0.8 [10] for a wide flow range and is known to be higher than ^{99m}Tc-labelled tracers such as tetrofosmine and sestamibi [29]. The physical characteristics of ^{201}Tl are unfortunately not ideal as low energy emission increases the attenuation factor and the scatter in the image. In addition, the relatively long half-life limits the administered activity to about a tenth of that with ^{99m}Tc tracers. Despite these shortcomings, the physiological characteristics of having high first-pass EF make ^{201}Tl an interesting tracer particularly for the absolute quantitation of MBF and the coronary flow reserve. This study demonstrates that quantitative physiological parameters can be derived from dynamic ^{201}Tl SPECT studies, despite its less than ideal imaging characteristics.

Whilst the quantitative physiological parameter estimation removed the systematic bias between MBF estimated by ^{201}Tl dynamic SPECT and by microspheres, the spread of data points around the regression line was rather large (Figs. 6e and 7c). This is not only due to possible errors in the estimation of MBF from the ^{201}Tl, but there was also considerable variation in flow estimated by the microspheres at the beginning and end of the study. Thus, at least part of the variability is attributable to errors in microsphere flow measurement, and particularly for the pharmaceutical intervention studies, flow may not have remained constant throughout the entire study duration, which may also account for some of the differences seen between the various flow measurements.

V_d estimated in this study could serve as an index of viability, as viable myocytes are required to maintain the large concentration gradient between plasma and myocardium at equilibrium. There was no significant difference in V_d values between rest, beta-blocker and adenosine studies when fitted for 1 h (Fig. 8). The significant difference between the 1- and 4-h fit for resting data could be explained by the limitation of the two-compartment model. Considerable spread in the V_d values observed over all dog studies on the other hand was partially attributed to the short (insufficient) scan time for reliable estimates of V_d. With the exception of the large, outlying V_d values in all 5 regions of 1 dog, the resting V_d values fell within a relatively narrow range of 47 to 65 (mean±SD=55±6). Given the sufficiently long scan time, significant reduction in V_d in infarcted areas may be detected. However, this would need to be tested with a suitable study design.

The scan time of 4 h required to achieve reliable V_d estimates is not practical in the routine clinical setting. As has been shown by Lau et al. [30], the scan period may be split into two sessions, an early dynamic scan for 30 min followed by a single static scan at approximately 3 h. This scheme is not more onerous than current rest/re-distribution protocols and hence could be practical. In addition, it may be possible to simplify the scanning protocol further to two static scans by using the table look-up method for the two-compartment model, which has been successfully employed for other SPECT tracers with relatively slow kinetics similar to ^{201}Tl [27, 31, 32]. This warrants further investigation.

This study relies on established, rigorous attenuation and scatter correction in SPECT [5] and availability of multi-detector SPECT systems capable of performing dynamic acquisition. To our knowledge, this is the first report that has demonstrated that it is possible to obtain quantitative physiological parameter estimates of K_1 and V_d in the myocardium using a clinical SPECT scanner and ^{201}Tl. This work suggests that it is feasible to apply our technique to clinical studies. Further studies are, however, needed to validate the proposed approach in the clinical setting. Incomplete motion correction is one possible error source, particularly in patients. Dynamic SPECT is probably more sensitive to the possible movement of patients during the study. Shortened clinical protocol is preferred, but this requires additional development to improve the reliability of parameter estimates. In addition, two scanning sessions are needed to assess the coronary flow reserve. We have recently demonstrated a technique to assess two cerebral blood flow images, one at rest and another after a vasodilating drug, from a single session of a SPECT scan in conjunction with split dose administration of ^{123}I-iodoamphetamine and dynamic SPECT [7]. As a clinical implication, the quantitative assessment of MBF and coronary flow reserve is important. For instance, coronary micro-vascular dysfunction or impaired endothelial function in patients with coronary risk factors or patients with cardiomyopathy or with heart failure is an un-resolved important issue to answer [11]. Coronary flow reserve can be reduced in patients with hypercholesterolemia without overt coronary stenosis [12]. A systematic study should be carried out to validate this approach for assessing MBF at rest and after adenosine from a single session of a scan.

Acknowledgement This study was supported by the Budget for Nuclear Research of the Ministry of Education, Culture, Sports, and Technology (MEXT), Japan; a grant from the Cooperative Link of Unique Science and Technology for Economy Revitalization promoted by the Ministry of Education, Culture, Sports and Technology, Japan and a grant for translational research from the Ministry of Health, Labour and Welfare (MHLW), Japan. We would like to thank Nihon Medi-Physics, Hyogo, Japan for providing the ^{201}Tl samples and also Mr. Yoshihide Takatani for his invaluable suggestion on the study design.

References

1. Gullberg GT, Huesman RH, Ross SG, et al. Dynamic cardiac single-photon emission computed tomography. In: Beller GA, Zaret BL, editors. Nuclear cardiology: state of the art and future directions. Philadelphia, PA: Mosby-Year Book Inc.; 1998. p. 137–87.
2. Chiao PC, Ficaro EP, Dayanikli F, Rogers WL, Schwaiger M. Compartmental analysis of technetium-99m-teboroxime kinetics employing fast dynamic SPECT at rest and stress. J Nucl Med 1994;35(8):1265–73.
3. Narita Y, Eberl S, Iida H, Hutton BF, Braun M, Nakamura T, et al. Monte Carlo and experimental evaluation of accuracy and noise properties of two scatter correction methods for SPECT. Phys Med Biol 1996;41(11):2481–96.
4. Narita Y, Iida H, Eberl S, Nakamura T. Monte Carlo evaluation of accuracy and noise properties of two scatter correction methods for ^{201}Tl cardiac SPECT. IEEE Trans Nucl Sci 1997;44:2465–72.
5. Iida H, Shoji Y, Sugawara S, Kinoshita T, Tamura Y, Narita Y, et al. Design and experimental validation of a quantitative myocardial ^{201}Tl SPECT System. IEEE Trans Nucl Sci 1999;46:720–6.
6. Iida H, Narita Y, Kado H, Kashikura A, Sugawara S, Shoji Y, et al. Effects of scatter and attenuation correction on quantitative assessment of regional cerebral blood flow with SPECT. J Nucl Med 1998;39(1):181–9.
7. Kim KM, Watabe H, Hayashi T, Hayashida K, Katafuchi T, Enomoto N, et al. Quantitative mapping of basal and vasareactive cerebral blood flow using split-dose ^{123}I-iodoamphetamine and single photon emission computed tomography. Neuroimage 2006;33(4):1126–35.
8. Beller GA, Watson DD, Pohost GM. Kinetics of thallium distribution and redistribution: clinical applications in sequential myocardial imaging. In: Pitt B, Strauss HW, editors. Cardiovascular nuclear medicine. St. Louis: Mosby; 1979. p 225–42.
9. Berman DS, Maddhi J, Garcia EV. Role of thallium-201 imaging in the diagnosis of myocardial ischemia and infarction. In: F HS, editor. Nuclear medicine annual. New York: Raven; 1980. p 1–55.
10. Weich HF, Strauss HW, Pitt B. The extraction of thallium-201 by the myocardium. Circulation 1977;56(2):188–91.
11. Camici PG, Crea F. Coronary microvascular dysfunction. N Engl J Med 2007;356(8):830–40.
12. Yokoyama I, Ohtake T, Momomura S, Nishikawa J, Sasaki Y, Omata M. Reduced coronary flow reserve in hypercholesterolemic patients without overt coronary stenosis. Circulation 1996;94 (12):3232–8.
13. Li J, Tsuji BMW, Welch A, Frey EC, Gullberg GT. Energy window optimization in simultaneous Technetium-99m and Thallium-201 SPECT data acquisition. IEEE Trans Nucl Sci 1995;42:1207–13.
14. Meikle SR, Hutton BF, Bailey DL. A transmission-dependent method for scatter correction in SPECT. J Nucl Med 1994;35(2):360–7.
15. Hudson HM, Larkin RS. Accelerated image reconstruction using srdered subsets of projection data. IEEE Trans Med Imag 1994;13:601–9.
16. Choi Y, Hawkins RA, Huang SC, Brunken RC, Hoh CK, Messa C, et al. Evaluation of the effect of glucose ingestion and kinetic model configurations of FDG in the normal liver. J Nucl Med 1994;35(5):818–23.
17. Hutton BF, Hudson HM, Beekman FJ. A clinical perspective of accelerated statistical reconstruction. Eur J Nucl Med 1997;24 (7):797–808.
18. Hutton BF, Lau YH. Application of distance-dependent resolution compensation and post-reconstruction filtering for myocardial SPECT. Phys Med Biol 1998;43(6):1679–93.
19. Pretorius PH, King MA, Pan TS, de Vries DJ, Glick SJ, Byrne CL. Reducing the influence of the partial volume effect on SPECT activity quantitation with 3D modelling of spatial resolution in iterative reconstruction. Phys Med Biol 1998;43(2): 407–20.
20. Soares EJ, Glick SJ, King MA. Noise chaeacterization of combined Bellini-type attenuation correction and frequency-distance principle restoration filtering SPECT. IEEE Trans Nucl Sci 1996;43:3278–90.
21. Iida H, Kanno I, Takahashi A, Miura S, Murakami M, Takahashi K, et al. Measurement of absolute myocardial blood flow with H215O and dynamic positron-emission tomography. Strategy for quantification in relation to the partial-volume effect. Circulation 1988;78(1):104–15.
22. Araujo LI, Lammertsma AA, Rhodes CG, McFalls EO, Iida H, Rechavia E, et al. Noninvasive quantification of regional myocardial blood flow in coronary artery disease with oxygen-15-labeled carbon dioxide inhalation and positron emission tomography. Circulation 1991;83(3):875–85.
23. Bergmann SR, Herrero P, Markham J, Weinheimer CJ, Walsh MN. Noninvasive quantitation of myocardial blood flow in human subjects with oxygen-15-labeled water and positron emission tomography. J Am Coll Cardiol 1989;14(3):639–52.
24. Iida H, Rhodes CG, de Silva R, Yamamoto Y, Araujo LI, Maseri A, et al. Myocardial tissue fraction-correction for partial volume effects and measure of tissue viability. J Nucl Med 1991;32(11): 2169–75.
25. Iida H, Tamura Y, Kitamura K, Bloomfield PM, Eberl S, Ono Y. Histochemical correlates of (15)O-water-perfusable tissue fraction in experimental canine studies of old myocardial infarction. J Nucl Med 2000;41(10):1737–45.
26. Iida H, Itoh H, Nakazawa M, Hatazawa J, Nishimura H, Onishi Y, et al. Quantitative mapping of regional cerebral blood flow using iodine-123-IMP and SPECT. J Nucl Med 1994;35(12):2019–30.
27. Onishi Y, Yonekura Y, Nishizawa S, Tanaka F, Okazawa H, Ishizu K, et al. Noninvasive quantification of iodine-123-iomazenil SPECT. J Nucl Med 1996;37(2):374–8.
28. Takikawa S, Dhawan V, Spetsieris P, Robeson W, Chaly T, Dahl R, et al. Noninvasive quantitative fluorodeoxyglucose PET studies with an estimated input function derived from a population-based arterial blood curve. Radiology 1993;188(1):131–6.
29. Fukushima K, Momose M, Kondo C, Kusakabe K, Kasanuki H. Myocardial kinetics of (201)Thallium, (99m)Tc-tetrofosmin, and (99m)Tc-sestamibi in an acute ischemia–reperfusion model using isolated rat heart. Ann Nucl Med 2007;21(5):267–73.
30. Lau CH, Eberl S, Feng D, Iida H, Lun PK, Siu WC, et al. Optimized acquisition time and image sampling for dynamic SPECT of Tl-201. IEEE Trans Med Imag 1998;17(3): 334–43.
31. Iida H, Itoh H, Bloomfield PM, Munaka M, Higano S, Murakami M, et al. A method to quantitate cerebral blood flow using a rotating gamma camera and iodine-123 iodoamphetamine with one blood sampling. Eur J Nucl Med 1994;21(10):1072–84.
32. Onishi Y, Yonekura Y, Mukai T, Nishizawa S, Tanaka F, Okazawa H, et al. Simple quantification of benzodiazepine receptor binding and ligand transport using iodine-123-iomazenil and two SPECT scans. J Nucl Med 1995;36(7):1201–10.